The Relationship between Downward Irradiance and Upper Ocean Structure

J. J. SIMPSON

Scripps Institution of Oceanography, La Jolla, CA 92093

T. D. DICKEY

Institute for Marine and Coastal Studies and Department of Geological Sciences, University of Southern California, Los Angeles 90007

(Manuscript received 15 May 1980, in final form 22 December 1980)

ABSTRACT

The relationship between downward irradiance and upper ocean structure has been studied using a numerical model. Two general classes of irradiance parameterizations were utilized. The first (case I) employed a single attenuation length while the second (case II) involved two attenuation lengths. The latter formulation provided for enhanced absorbance in the upper few meters. Wind speeds of 0, 1, 2, 3, 4, 5, 10 and 20 m s^{-1} were used for the simulations in order to characterize heat versus wind dominated regimes. A one-dimensional second moment turbulent closure model was selected for the study so that heat could be treated differentially with depth. The case II results indicated warmer surface temperatures, shallower mixed layers, and more intense thermoclines than case I for wind speeds < 10 m s^{-1}. Results converged for higher wind speeds. There was considerably greater sensitivity to wind speed for case II when compared with case I. Mean horizontal velocity as well as thermal structure was sensitive to the empirical formulation of downward irradiance. For low wind speeds the turbulent energy budget is dominated by shear production, dissipation and the diffusion of turbulent kinetic energy, regardless of parameterization. For high wind speeds, shear production is balanced by dissipation. The results of this study provide strong indications that downward irradiance and its proper parameterization are important in determining upper ocean structure and may have implications for large-scale climate studies.

1. Introduction

The response of the upper ocean to meteorological forcing has been studied most often as a locally generated process and has resulted in two distinct types of one-dimensional mixed layer models. One type, known as an integral model (Kraus and Rooth, 1961; Kraus and Turner, 1967; Geisler and Kraus, 1969; Kitaigorodsky and Miropolsky, 1970; Denman, 1973; Denman and Miyake, 1973; Pollard *et al.*, 1973; Niiler, 1975; Gill and Turner, 1976; Thompson, 1976), assumes that the actively mixing upper layer is homogeneous. Solutions are obtained from energy balance considerations in this uniformly well-mixed layer. Computationally, this approach is economical. However, Mellor and Durbin (1975) and Kondo *et al.* (1979) have pointed out that such models do not predict the existence of a well-mixed layer as a result of oceanic boundary conditions but rather assume its existence *a priori*. The second type, generally known as a turbulence closure model (Mellor and Durbin, 1975; Marchuk *et al.*, 1977; Madsen, 1977; Kondo *et al.*, 1979; Kundu, 1980), uses a complete set of turbulence and thermodynamic equations to predict from the oceanic boundary conditions the detailed thermal and velocity structure in the upper ocean. This approach is more expensive computationally and requires particular hypotheses and assumptions to complete the closure. Reviews of these models may be found in Kraus (1977) and in Garwood (1979). With the exception of Kondo *et al.* (1979), all of these models either have parameterized the penetrative component of the solar radiation with an exponential empirical form or they have neglected it. However, recent measurements of downward irradiance (Paulson and Simpson, 1977) suggest that the commonly used exponential decay law for the absorbance of solar radiation in the upper ocean may be inappropriate. For these reasons, the relationship between the penetrative component of solar radiation and upper ocean structure has not been resolved.

The sensitivity of several models to the parameterization of solar penetration has been studied. For example, Kraus and Turner (1967) point out that the predicted minimum depth of the summer thermocline under seasonally typical conditions ($U_{10} = 8$ m s^{-1} and $I_0 = 2.5 \times 10^7$ J m^{-2} day^{-1}) was 87 m when an attenuation length of 20 m was used. For an attenuation length of 10 m, the predicted minimum depth of the summer thermocline still was unusually deep at 57 m. Kraus and Turner con-

0022-3670/81/030309-15$07.75

cluded that under summertime conditions the effects of radiation are likely to dominate those of mechanical stirring. Denman (1973) generalized the Kraus-Turner (1967) model to investigate the time-dependent behavior of the upper ocean in response to meteorological forcing on time scales from one to several days. Denman found that increasing the attenuation length by a factor of 2 (allowing the solar radiation to penetrate to greater depths) resulted in a 70% increase in mixed-layer depth. Alexander and Kim (1976) used the Kraus-Turner (1967) one-dimensional model, in diagnostic form, to calculate oceanic mixed-layer depths for the summertime North Pacific. They found that the calculated mixed-layer depths tended to differ quantitatively from observed values by as much as an order of magnitude, and that the results were rather sensitive to the value of the attenuation length used.

Mellor and Durbin (1975) used a second moment turbulent closure scheme (Mellor, 1973; Mellor and Yamada, 1974) to simulate Ocean Station Papa data. The level 2 version was used for this simulation, and neither the effects of solar penetration nor the diffusion of turbulent kinetic energy were included. The results of the simulation agree well with the observations. It should be noted, however, that this simulation was done under conditions where wind stirring presumably dominated convective processes (see Denman and Miyake, 1973, Fig. 2).

The purpose of the present study is to determine the effect of solar flux divergence on upper ocean structure under various wind-forcing conditions using a series of downward irradiance parameterizations. The level 2½ version of the Mellor and Yamada (1974) turbulent closure scheme (e.g., Yamada, 1977; Blumberg and Mellor, 1981) was chosen for the present study. This model was selected primarily on the basis of its capacity to distribute downward irradiance differentially throughout the water column rather than in an integrated fashion as would be required by an integral model.

2. Downward irradiance

Several of the one-dimensional models discussed above have been used to predict the temperature of the sea surface and the depths of both the diurnal and seasonal thermocline. In most cases where comparisons with observations have been made (e.g., Denman, 1973), the absorbance of downward irradiance has been assumed to be an exponential function of depth given by

$$I(z) = I_0 \exp(z/\zeta_1), \quad (1)$$

where $I(z)$, the downward irradiance, is the radiant flux density on a horizontal surface due to contributions from the entire upward hemisphere, I_0 is the incident less reflected and emergent irradiance at the surface, z is the vertical coordinate, positive upward with origin at mean sea level, and ζ_1 is the attenuation length, assumed constant with depth. The assumption of an exponential decay with depth is a poor approximation in the upper 10 m of the ocean (Sverdrup *et al.*, 1942; Jerlov, 1968; Kondo and Watabe, 1969) because of the preferential absorption of the short- and longwave components of light. Below a depth of 10 m, however, the assumption of exponential decay is a good approximation because selective absorption has left only blue-green light. These facts, while well known, have not always been completely taken into account when modeling the upper ocean.

Recent observations of downward irradiance as a function of depth (Paulson and Simpson, 1977) showed that irradiance decreases more rapidly with depth than predicted by (1) for the upper few meters, falling to approximately one-third the incident value between 2 and 3 m depth. These latter observations suggest that a more appropriate parameterization of the absorbance of downward irradiance is given by

$$I(z) = I_0[R \exp(z/\zeta_1) + (1 - R) \exp(z/\zeta_2)], \quad (2)$$

where ζ_1 and ζ_2 are attenuation lengths and R is an empirical constant. This form was originally suggested by Kraus (1972). Preferential absorption of the longwave (red) spectral components in the upper few meters is characterized by the first term in (2) while absorption of the visible (blue-green) spectral components below a depth of 10 m is characterized by the second term (i.e., $\zeta_2 > \zeta_1$).

A scheme for classifying oceanic water according to its clarity was introduced by Jerlov (1968). He defined five types of water which ranged from clear to increasingly turbid water. The latter water type is most appropriate for biologically productive coastal waters. Values of the irradiance constants for the water types considered in this study are given in Table I. Profiles of downward irradiance for these water types, calculated using Eqs. (1) and (2), are shown in Fig. 1. A simple e-folding length cannot be associated with (2) as can be seen from the vertical distribution of absorbance in the upper 20 m. In the limit of small z the length scale associated with the first term in (2) dominates, while below a depth of about 8 m the length scale associated with the second term in (2) dominates. A transition between the two regimes occurs between 2 and 10 m. Its particular value is dependent on the irradiance constants R, ζ_1 and ζ_2 associated with a given water type. The value of irradiance at depth ($z > 10$ m) is also inappropriate when Eq. (1) is used since the value of $I(z) \neq I_0$ when extrapolated to the surface. The divergence of downward irradiance may be written as

$$Q(z) = \frac{\partial I}{\partial z}. \quad (3)$$

TABLE 1. Empirical forms used to test the sensitivity of the upper ocean structure to the parameterization of the absorption of downward irradiance.

		R	ζ_1 (m)	ζ_2 (m)
Single exponential: $I(z) = I_0 \exp(z/\zeta_1)$				
Typically used (Denman, 1973; Alexander and Kim, 1976)	Type I	—	10	—
	Type II	—	5	—
Double exponential: $I(z) = I_0[R \exp(z/\zeta_1) + (1 - R) \exp(z/\zeta_2)]$				
Paulson and Simpson (1977)	Type I	0.580	0.35	23
	Type III	0.780	1.4	7.9

Profiles of $Q(z)$ for the water types given in Table 1 are shown in Fig. 2. These profiles clearly suggest that different empirical forms of downward irradiance $I(z)$ may lead to significantly different upper ocean temperature structure [see Eq. (7)].

3. The model

The level 2½ version of the Mellor-Yamada turbulent closure scheme was modified to account for solar flux divergence. The details of the closure may be found in Blumberg and Mellor (1981); however, a brief description of the model will be included for completeness. The mean zonal and meridional momentum equations are

$$\frac{\partial U}{\partial t} - f(V - V_g) = \frac{\partial}{\partial z}(-\overline{u'w'}), \tag{4}$$

$$\frac{\partial V}{\partial t} + f(U - U_g) = \frac{\partial}{\partial z}(-\overline{v'w'}), \tag{5}$$

where U and V are the mean zonal and meridional velocity components, U_g and V_g are the corresponding geostrophic velocities, $\overline{u'w'}$ and $\overline{v'w'}$ are the vertical turbulent Reynolds stresses, f is the Coriolis

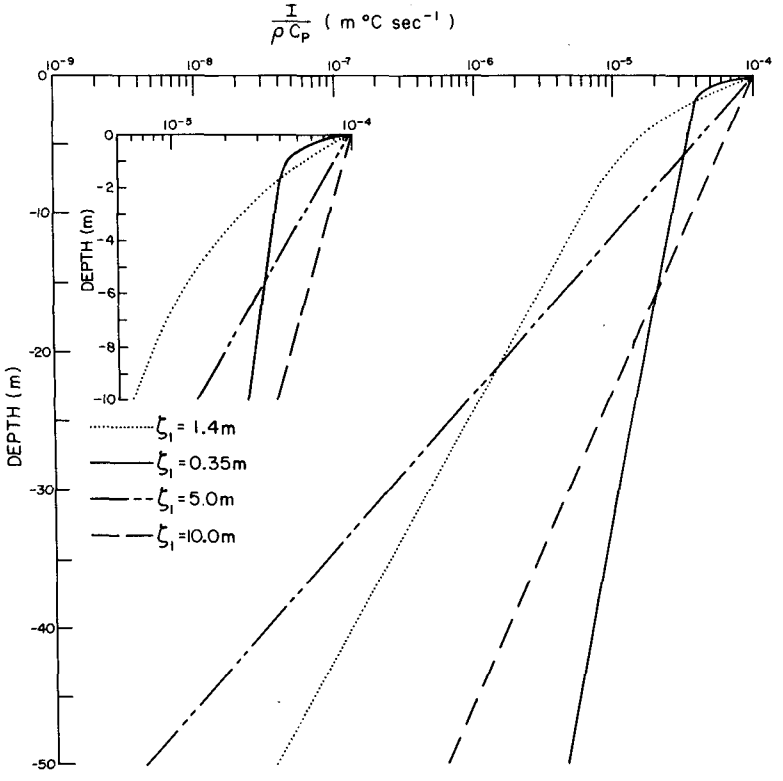

FIG. 1. Vertical profiles of downward irradiance for the parameterizations given in Table 1. The profiles in this and subsequent figures are identified by the attenuation length scale ζ_1. Profiles for $\zeta_1 = 5$ m and $\zeta_1 = 10$ m were calculated using Eq. (1). The remaining profiles were calculated using Eq. (2).

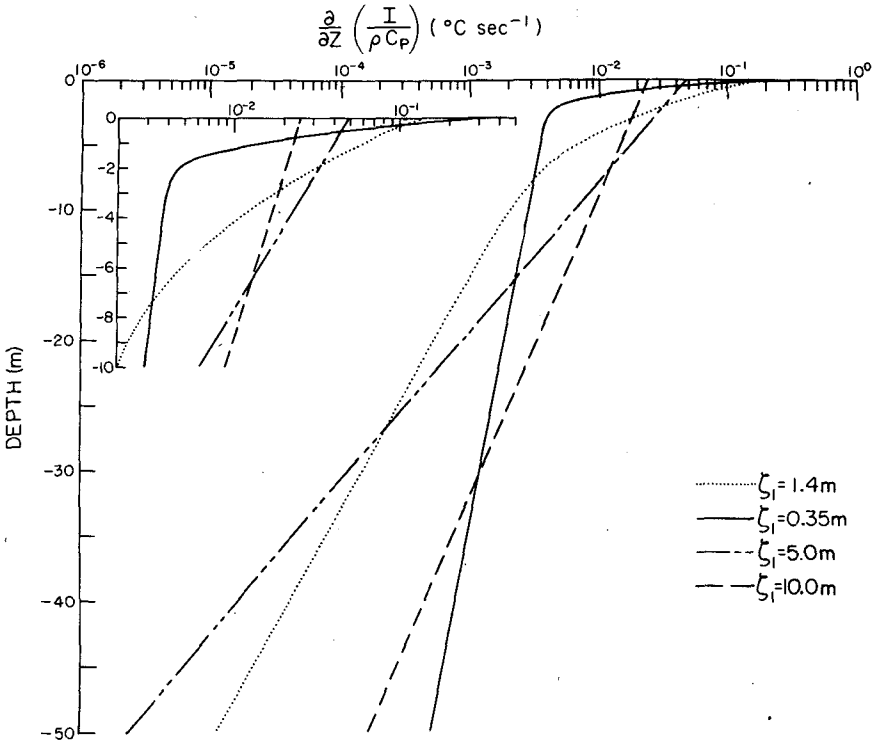

FIG. 2. Vertical profiles of the divergence of downward irradiance [see Eq. (3)] corresponding to the irradiance profiles of Fig. 1.

parameter and t time. The mean vertical velocity is assumed to be zero and hydrostatic balance is given by

$$\frac{\partial P}{\partial z} = -\rho g, \tag{6}$$

where P is the mean pressure, ρ is the *in situ* density, and g is the acceleration due to gravity. Incompressibility is assumed, and an equation of state is used to determine density. The Boussinesq approximation is used. Omission of the advection terms in the momentum equations is based on the assumption of a low Rossby number regime. The horizontal divergence of turbulent Reynolds stress terms is neglected because variability in the vertical is assumed to be much greater than that in the horizontal. The heat conservation equation differs from the one used by Mellor and Durbin (1975) and by Blumberg and Mellor (1981) because the divergence of the downward irradiance is included. The equation may be written in the form

$$\rho c_p \frac{\partial T}{\partial t} + \rho c_p \frac{\partial}{\partial z}\overline{w'T'} = Q(z) = \frac{\partial I}{\partial z}, \tag{7}$$

where T is the mean temperature and c_p is the specific heat of sea water. The first term is the local rate of change of heat, the second term is the vertical divergence of turbulent heat flux, and the right-hand side of (7) is the vertical divergence of the downward irradiance flux. The conservation of salt may be included in the model. However, for the present study salinity was assumed to be uniform in space and time. Turbulent kinetic energy, $\frac{1}{2}q^2 = \frac{1}{2}(\overline{u'^2} + \overline{v'^2} + \overline{w'^2})$, and a turbulent length scale l are computed. The level 2½ version used for these calculations includes the diffusion of turbulent kinetic energy, which appears to be important for low wind-speed situations. The equation for the turbulent kinetic energy may be written as

$$\text{TEND} + \text{DIFF} = \text{SPROD} + \text{BPROD} - \text{DISS}, \tag{8}$$

where

$$\text{TEND} = \frac{\partial q^2/2}{\partial t},$$

$$\text{DIFF} = \partial/\partial z(\overline{w'q^2/2}),$$

$$\text{SPROD} = -\overline{u'w'}\frac{\partial U}{\partial z} - \overline{v'w'}\frac{\partial V}{\partial z},$$

$$\text{BPROD} = -\frac{g}{\bar{\rho}}\overline{w'\rho'}.$$

TEND is the tendency of turbulent kinetic energy, DIFF is the diffusion of turbulent kinetic energy, SPROD is the shear production, BPROD is the buoyancy production and DISS is the dissipation.

The problem is closed by using hypotheses and assumptions concerning third moment terms (e.g., Mellor, 1973). Requisite empirical constants are determined from laboratory flow and are not adjusted. While the details of the model are rather involved, it is possible to reduce the turbulent Reynolds stress and heat flux terms to the following expressions:

$$-\overline{u'w'} = qlS_M(\mathrm{Ri}_f)\frac{\partial U}{\partial z}, \tag{9}$$

$$-\overline{v'w'} = qlS_M(\mathrm{Ri}_f)\frac{\partial V}{\partial z}, \tag{10}$$

$$-\rho c_p\overline{w'T'} = \rho c_p qlS_H(\mathrm{Ri}_f)\frac{\partial T}{\partial z}. \tag{11}$$

S_M and S_H are stability functions. The flux Richardson number is defined as

$$\mathrm{Ri}_f = \frac{g\bar{\rho}^{-1}\overline{w'\rho'}}{-\overline{u'w'}\dfrac{\partial U}{\partial z} - \overline{v'w'}\dfrac{\partial V}{\partial z}}. \tag{12}$$

This expression is simply the ratio of negative turbulent buoyancy production to shear production. An important feature is the extinction of turbulence ($S_M = S_H = 0$) for $\mathrm{Ri}_f > 0.21$ (e.g, see Fig. 6 of Mellor, 1973). The numerical scheme employs a two time step implicit algorithm (Richtmyer and Morton, 1967). The vertical grid spacing is optimized by using a logarithmic distribution. This is ideal for the input of the penetrative component of solar irradiance. There are 101 levels for the upper 50 m with the density of grid points being greatest near the surface. The time step is one hour. Simulations are run for 72 h and effects of spin up are observed during the first few hours.

The boundary conditions for the model include

1) wind stress τ_{ox}, τ_{oy}:

$$\tau_{ox} = \rho qlS_M(\mathrm{Ri}_f)\partial U/\partial z\big|_{z=0} \tag{13}$$

$$\tau_{oy} = \rho qlS_M(\mathrm{Ri}_f)\partial V/\partial z\big|_{z=0}. \tag{14}$$

2) turbulent heat flux H:

$$H = \rho c_p qlS_H(\mathrm{Ri}_f)\frac{\partial T}{\partial z}\bigg|_{z=0}. \tag{15}$$

The problem is initialized with specified temperature and horizontal velocity profiles.

4. Model results

The purpose of the following computations is to determine the effect of the divergence of downward irradiance on upper ocean structure under a broad range of wind stress conditions using a series of irradiance parameterizations (Table 1). The conditions common to all runs are shown in Table 2. The wind stress was determined from the empirical equation

$$\tau_{ox} = \rho_a C_{10} U_{10}^2, \tag{16}$$

where ρ_a is the density of air, C_{10} is the drag coefficient, and U_{10} is the mean zonal wind velocity at 10 m above the air-sea interface. The values of I_0 and H were chosen from mid-ocean observations made during the winter (Simpson and Paulson, 1977, and 1979). Climatologically higher values for I_0 (List, 1951) are characteristic of summertime conditions. The geostrophic velocity was assumed to be zero and the water column was initially at rest. The wind and radiation conditions were imposed at the beginning of the simulations and remained unchanged throughout the experiment. The latitude is that of Ocean Station Papa and the initial temperature profile was chosen from Ocean Station Papa data (see Mellor and Durbin, 1975). The wind speeds used for the study were $U_{10} = 0$, 1, 2, 3, 4, 5, 10 and 20 m s^{-1}. The various parameterizations of downward irradiance are identified by the attenuation length ζ_1. The main intent of the present calculations is to identify possible significant variations in upper ocean structure caused by the aforementioned processes rather than to simulate a particular condition. Hence, the effects of solar altitude and refraction at the sea surface are neglected. Such effects are more germane to diurnal and seasonal studies. The diurnal studies are near completion. Furthermore, the model does not include wind-wave energy fluxes; however, it has been noted by Kundu (1980) that such an omission does not significantly affect the mixed-layer dynamics.

TABLE 2. Conditions for sensitivity study runs.

Parameter	Symbol	Value
Surface turbulent heat flux	H	8.16×10^1 J m^{-2} s^{-1}
Geostrophic velocity	U_g, V_g	0
Initial mean velocity	U, V	0
Coriolis parameter	f	1×10^{-4} s^{-1}
Salinity	S	35.0‰
Drag coefficient	C_{10}	1.4×10^{-3}
Specific heat of water	c_p	4.0×10^3 J Kg^{-1} °C^{-1}
Density of air	ρ_a	1.26 Kg m^{-3}
Net downward irradiance at the surface	I_0	4.08×10^2 J m^{-2} s^{-1}

The temperature structure for the zero wind-speed case ($U_{10} = 0$) is shown in Fig. 3 for all parameterizations. The validity of the model for the zero wind speed case has been shown by Mellor and Yamada (1977). The initial profile and subsequent profiles at $t = 12$, 18 and 24 h are given. In the following discussion parameterizations based on (1) are referred to as case I and those based on (2) are referred to as case II. The mean temperature structure associated with case II indicates warmer sea surface tem-

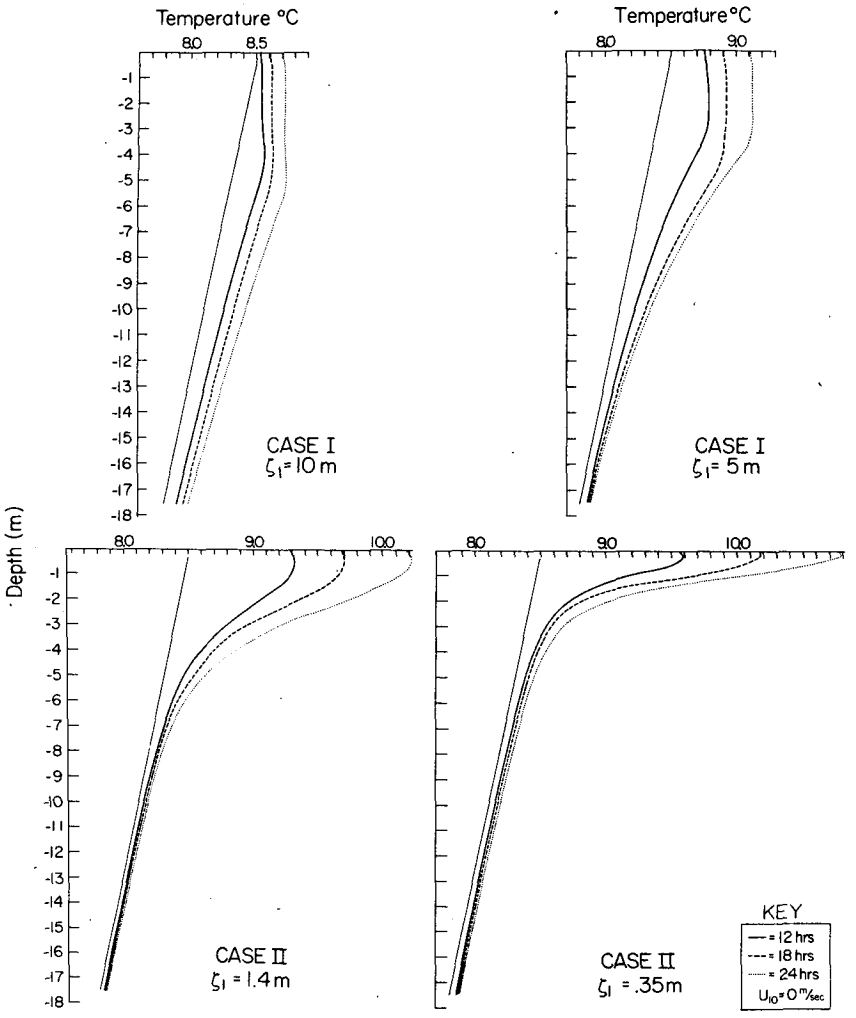

FIG. 3. The initial temperature profile and subsequent profiles at t = 12, 18 and 24 h are shown for all parameterizations. The wind speed for these runs is 0 m s^{-1}.

perature, shallower mixed-layer depths and a more intense thermocline when compared with case I. Analogous profiles for a wind speed of 2 m s^{-1} are shown in Fig. 4. The qualitative features are quite similar to those shown in Fig. 3. For case I there is little difference between the temperature structure resulting from 0 to 2 m s^{-1} winds. For case II (ζ_1 = 1.4 m), however, the sea surface temperature is slightly cooler ($\Delta T \sim 0.1$°C) for U_{10} = 2 m s^{-1} than for U_{10} = 0 m s^{-1}. The most significant change in thermal structure occurred for case II (ζ_1 = 0.35 m) where the sea surface temperature decreased by 0.8°C and the mixed-layer depth increased by 50% when the wind speed was increased from 0 to 2 m s^{-1}.

Temperature profiles for both cases under relatively high wind-speed conditions (U_{10} = 10 m s^{-1}) are shown in Fig. 5. For case I, the sea surface temperature decreased ($\Delta T \sim 0.3$°C for ζ_1 = 10 m and $\Delta T \sim 0.6$°C for ζ_1 = 5 m) after 24 h when compared with the zero wind-speed case. For case II, the sea surface temperature changes over the same time interval are much greater (e.g., for ζ_1 = 1.4 m, $\Delta T \sim 1.6$°C; and for ζ_1 = 0.35 m, $\Delta T \sim 2.3$°C). For this wind speed it should be noted that the mixed layer depth after 24 h is approximately 18 m for all parameterizations. At this depth the transition from ζ_1 to ζ_2 dominance has occurred for all parameterizations (see Fig. 2). A further indication of this transition is seen in Fig. 5 where case II with ζ_2 = 7.9 m and ζ_1 = 1.4 m shows a shallower mixed layer at 24 h compared to case II with ζ_2 = 23 m and ζ_1 = 0.35 m. This appears to explain the relative change in sea surface temperature associated with each of the parameterizations.

Small scale temperature inversions, with amplitudes typically <0.005°C, are seen in some of the

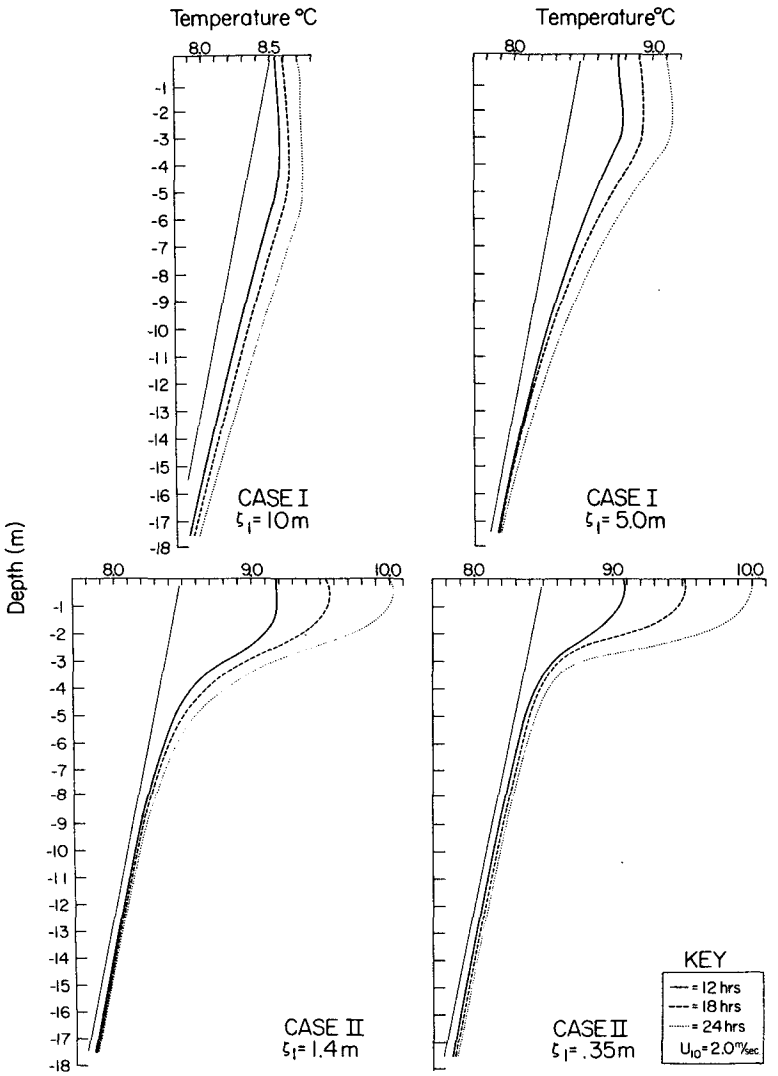

FIG. 4. As in Fig. 3 except for $U_{10} = 2$ m s^{-1}.

temperature profiles associated with the low wind-speed simulations. These inversions occur regardless of parameterization but are more pronounced for case II simulations. The depth at which the inversions occur scales with ζ_1. These inversions result from the combined effects of cooling at the surface due to sensible, latent and net longwave radiative heat transfer and the differential absorption of solar radiation at depth. Eckart (1968) observed the presence of shallow temperature inversions, similar to those in Figs. 3 and 4, in open ocean bathythermographs taken during the summer under low wind speeds. He concluded that these inversions resulted from the combined effects of daytime heating and nighttime cooling. He postulated that such inversions required an upward transfer of heat but noted that the magnitude of these thermal gradients was very small and would generally escape detection.

Such temperature inversions are gravitationally unstable and cannot persist for long periods of time. Even under zero wind-speed conditions, buoyancy forces work to reestablish a stable density profile. To determine the effects of buoyancy flux ($(g/\bar{\rho}) \times \overline{w'\rho'}$) we ran a simulation for 26 h under conditions identical to those in Table 2. Thereafter, all wind and heating were set to zero. Profiles of temperature, density and buoyancy flux for the interval 24–32 h of this simulation are shown in Fig. 6. Initially ($t = 24$ and 26 h), small inversions are present in the temperature profile. The differential absorption of heat at depth produces the sign reversals

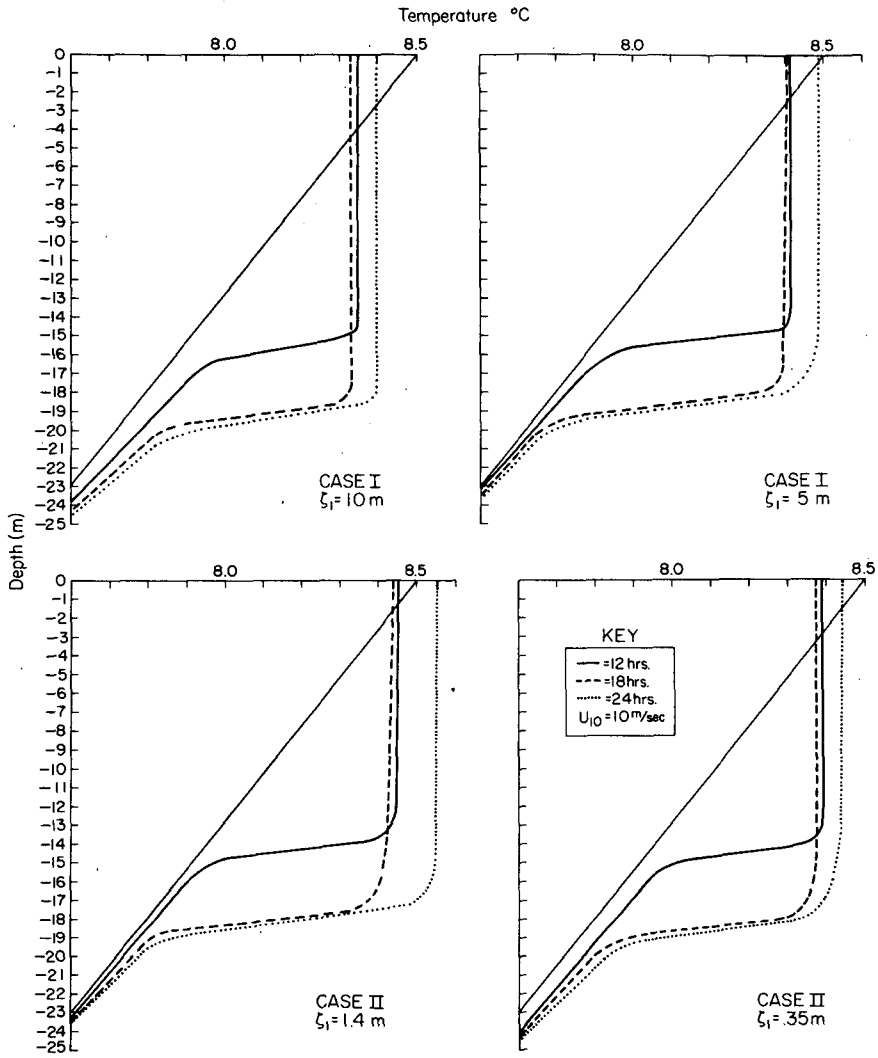

FIG. 5. As in Fig. 3 except for $U_{10} = 10$ m s^{-1}.

in the buoyancy flux (downward versus upward fluxes). The inversion corresponds spatially with the shallow region of negative buoyancy flux shown in Fig. 6. At $t = 28$ h the magnitude of the inversion has decreased and by $t = 30$ h the buoyancy flux has completely destroyed the inversion. Notice that the profile of buoyancy flux for $t = 30$ h is entirely positive. These results show that buoyancy forces alone produce a stable stratification over comparatively short time scales. Our results are consistent with both the observations and interpretation given by Eckart (1968) and by Clay and Medwin (1977, pp. 4–6).

Surface temperatures as functions of time are shown in Fig. 7 for the first 72 h for all irradiance parameterizations. The wind speeds were 0, 1, 2, 3, 4, 5, 10 and 20 m s^{-1}. Some parameterizations show more sensitivity to wind speed than others. For example, case I (i.e., $\zeta_1 = 5$ m and $\zeta_1 = 10$ m) show no appreciable change in sea surface temperature for wind speeds < 5 m s^{-1}. At a wind speed of 5 m s^{-1}, the change in sea surface temperature relative to the zero wind speed case for $\zeta_1 = 10$ m is extremely small ($\Delta T \sim 0.05$°C). Between 0 and 1 m s^{-1} there is little change in sea surface temperature for all case II parameterizations. However, at wind speeds > 1 m s^{-1}, increased wind speed results in a significantly decreased sea surface temperature. One interesting feature associated with these computed sea surface temperatures is the change in the relative order of given curves within a family. For example, between wind speeds of $U_{10} = 1$ m s^{-1} and $U_{10} = 3$ m s^{-1}, the curves associated with $\zeta_1 = 1.4$ m and $\zeta_1 = 0.35$ m exchange

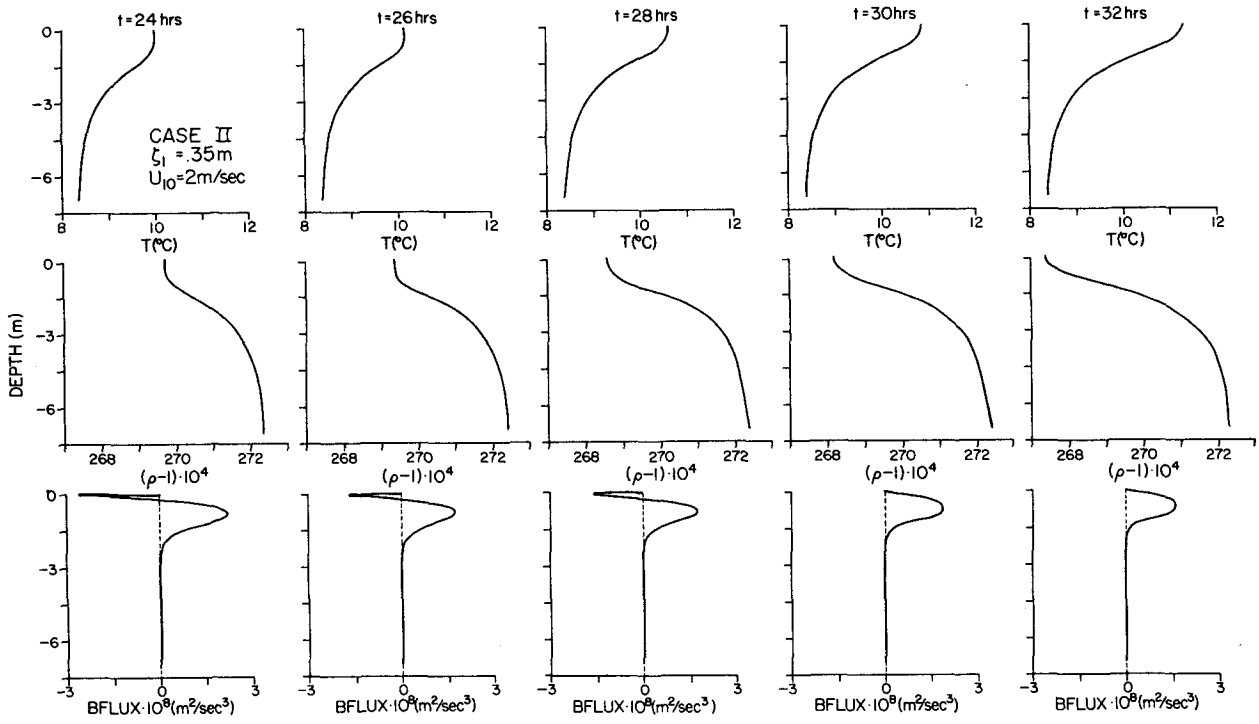

FIG. 6. Profiles of temperature, density and buoyancy flux. After t = 26 h all wind and heating were set to zero.

relative positions. At a wind speed of 1 m s^{-1}, the ζ_1 = 0.35 m parameterization results in a relatively warmer sea surface temperature when compared with the ζ_1 = 1.4 m parameterization. However, the reverse is true at 3 m s^{-1}. Changes in relative positions of curves continue for wind speeds up to 10 m s^{-1}. A possible explanation for this is the complex interplay between mixed-layer depth and the vertical dependence of the divergence of the downward irradiance. For the wind dominated regime (U_{10} = 20 m s^{-1}), the sea surface temperatures collapse to within 0.1°C of each other. A clear transition from an increase to a decrease in sea surface temperature occurs between U_{10} = 10 and 20 m s^{-1}. This indicates that the wind-dominated regime occurs for wind speeds in excess of 10 m s^{-1}.

Some models have omitted the penetrative component of solar radiation as previously noted. In these instances, all heating or cooling is presumed to take place at the surface. Simulations using this boundary condition and the parameter values given in Table 2 are included in Fig. 7 with the runs identified by the symbol δ. Extremely high surface temperatures are predicted for low wind speeds. For relatively high wind speeds (U_{10} = 10 m s^{-1}) simulations using this boundary condition are in agreement with the other parameterizations.

Sea surface temperatures as functions of time for given parameterizations (ζ_1 = 10, 5 and 1.4 m) are shown in Figs. 8a–8c for wind speeds of 0, 1, 2, 3, 4, 5, 10 and 20 m s^{-1}. Case I, ζ_1 = 10 m, shows little sensitivity to wind speed. For wind speeds < 5 m s^{-1}, there is relatively little difference in sea surface temperature for case I, ζ_1 = 5 m. The greatest sensitivity to wind speed is found with the case II parameterizations as seen in Fig. 8c (ζ_1 = 1.4 m).

Mixed-layer depths as functions of time are shown in Figs. 9a–9c for all parameterizations with wind speeds of 0, 10 and 20 m s^{-1}. The mixed layer depth was defined as the depth at which the temperature changed by 0.01°C over 0.2 m for the upper 1 m and over 0.05°C for depths greater than 1 m. The deepest mixed layer corresponds to the lowest sea surface temperature (Fig. 7) as expected. Relative changes of mixed-layer depth curves within the family are consistent with the corresponding changes in sea surface temperature curves noted previously. It may be noted that at U_{10} = 20 m s^{-1} the deepest mixed layer occurs for the largest of all attenuation length scales (e.g., case II, type 1, ζ_2 = 23 m).

In addition to the previously mentioned differences in temperature structure associated with various irradiance parameterizations, there are corresponding differences in the vertical profiles of horizontal velocity structure. Profiles of the mean zonal and meridional velocities after 72 hours with a uniform wind speed of 2 m s^{-1} are shown in Fig. 10a and 10b, respectively. The irradiance param-

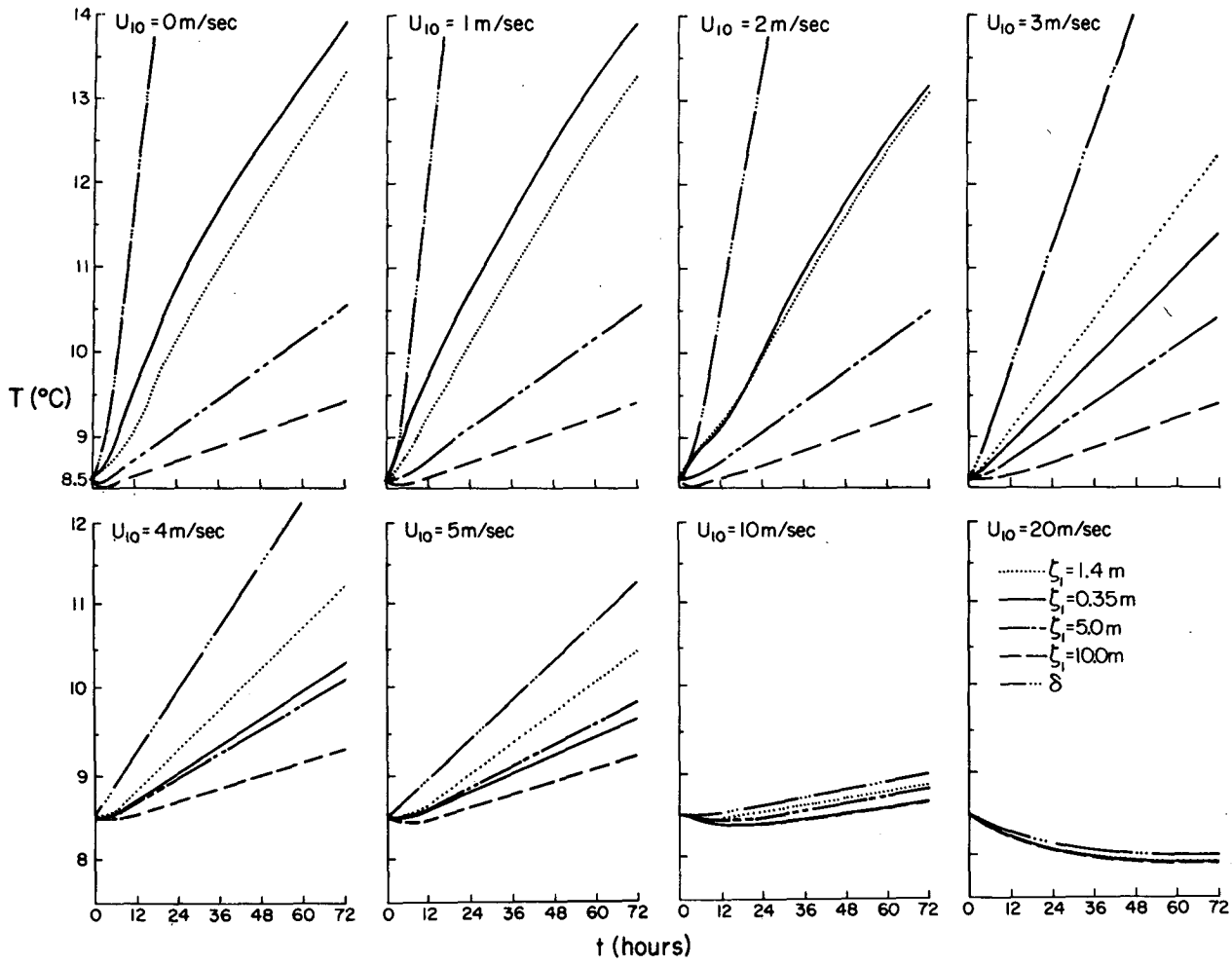

FIG. 7. Computed surface temperatures as functions of time for the first 72 h for all irradiance parameterizations are shown for different wind speeds.

eters corresponding to these profiles are case I (ζ_1 = 10 m) and case II (ζ_1 = 1.4 m). Significant differences in the horizontal velocity structure exist between the two cases. These may be explained at least in part by the significant differences in density structure. The magnitude of the mean velocities decreases as the mixed layer depth increases. Analogous velocity profiles for the high wind speed case (U_{10} = 20 m s^{-1}) are shown in Figs. 11a and 11b. At these wind speeds the profiles of horizontal velocity are nearly independent of irradiance parameterization.

The physical interpretation of the various runs can best be presented by considering several of the dynamically important parameters. Vertical profiles of T, Ri, K_H, BFLUX and the turbulent energy budget are shown in Fig. 12 for each water type at 24 h for a low wind speed (U_{10} = 2 m s^{-1}). The vertical eddy diffusivity of heat is represented by K_H. The buoyancy flux, BFLUX, is given by $g\bar{\rho}^{-1}\overline{w'\rho'}$. Considerable variability in the temperature structure (see Fig. 12) occurs among the four low wind speed simulations. Case I thermal structure is characterized by a deeper, colder mixed layer and bounded by a less intense thermal gradient compared to case II. Within this set of simulations shallower mixed layers correspond to smaller values of ζ_1. Similarly, vertical profiles of flux Richardson number and eddy diffusivity reflect the same general ordering with respect to the ζ_1 parameter. The Richardson number is <0.21 throughout the mixed layer and increases rapidly at the base of the mixed layer. The vertical distribution of K_H exhibits a subsurface maxima whose magnitude is determined primarily by the length scale ζ_1. The maximum in K_H corresponds to a region of minimum shear which occurs in the center portion of the mixed layer. This type of feature has been observed by

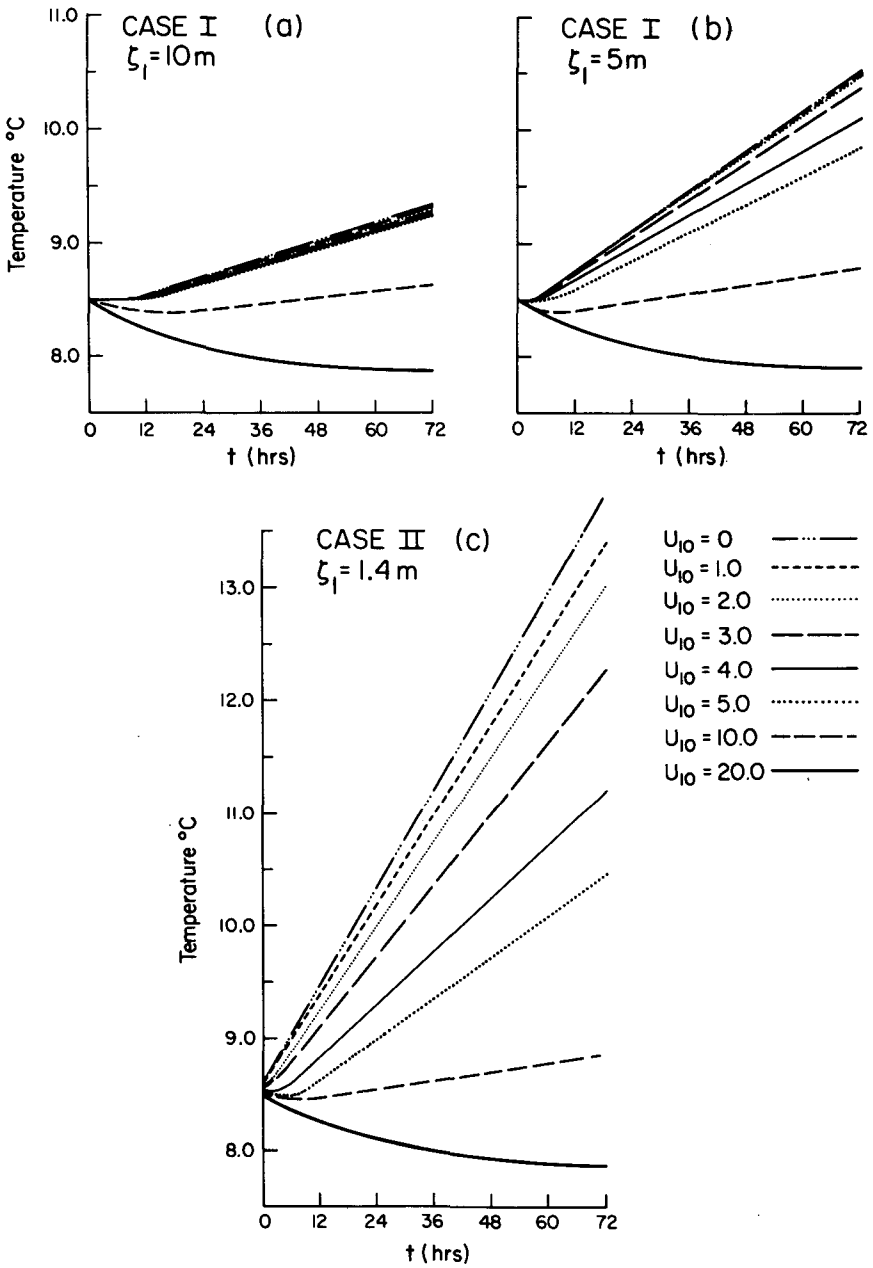

FIG. 8. Computed surface temperatures as functions of time for given parameterizations. Wind speed is in m s^{-1}.

McPhee and Smith (1976) and simulated by Kondo *et al.* (1979) and Kundu (1980). Vertical profiles of the buoyancy flux are negative throughout the mixed layer and into the thermocline for the case I simulations. This corresponds to a net decrease in the potential energy of the mixed layer. Case II simulations show a corresponding downward (negative) flux of buoyancy throughout a depth approaching that of the mixed layer. However, for the case II simulations, the buoyancy flux is upward (positive) within the upper region of the thermocline. For case II simulations, more pronounced shear zones at the base of the mixed layer result in increased entrainment of cold water. This leads to an upward (positive) flux of buoyancy and an increase in the mean potential energy of that portion of the water column. The different vertical distributions of potential energy associated with the case I and case II

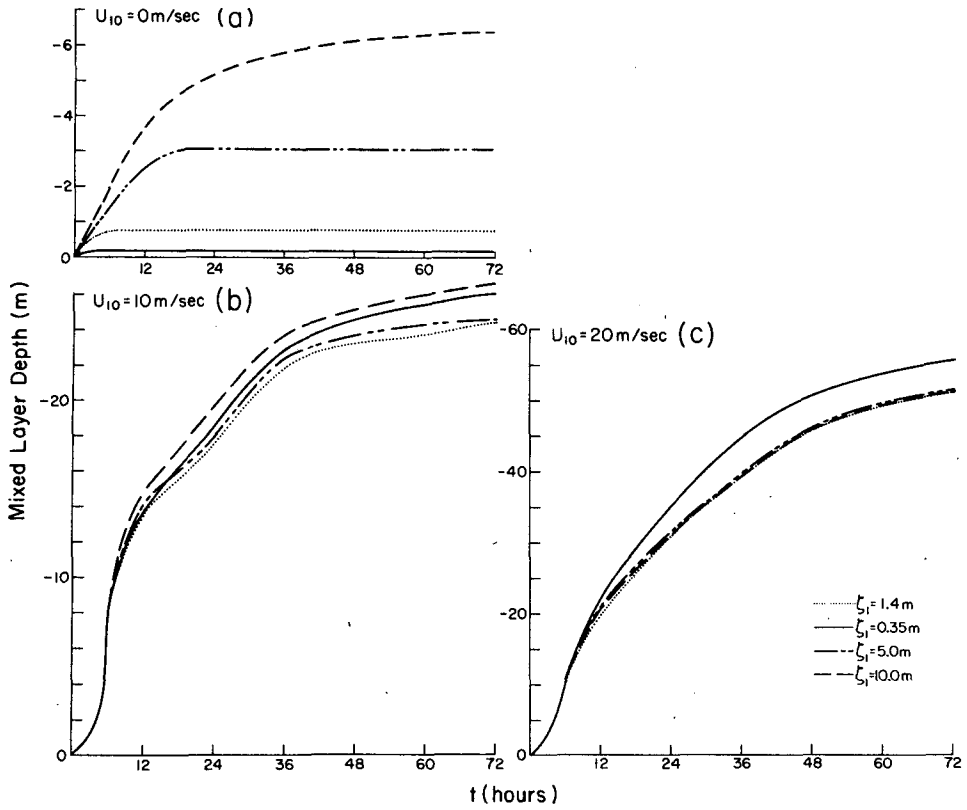

FIG. 9. Mixed-layer depths as functions of time for different wind speeds are shown.

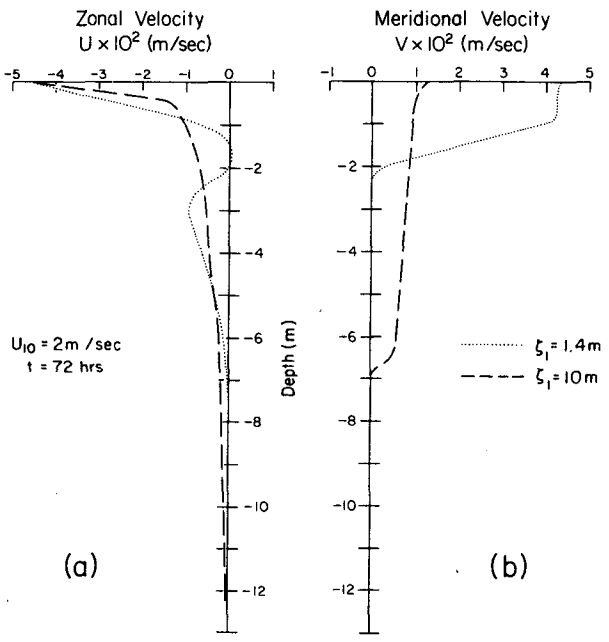

FIG. 10. Profiles of the mean zonal and meridional velocity after 72 hours with a uniform speed of 2 m s^{-1} for two different irradiance parameterizations are shown.

simulations result from the more intense entrainment and shallower absorption of heat associated with the case II parameterizations. The more dynamically complex profiles of case II probably result from the interplay among the mixed-layer depth and the length scales ζ_1 and ζ_2. The turbulent energy equation for low wind speeds is dominated by shear production, dissipation and turbulent diffusion. Tendency and buoyancy production are relatively insignificant. Below the depth of the mixed layer all terms approach zero.

The temperature structure and all other variables discussed previously for the high wind speed case are essentially identical regardless of parameterization. Representative profiles of two of the more interesting variables corresponding to case II (ζ_1 = 0.35 m) are shown in Fig. 13. The buoyancy flux profiles exhibit a pronounced positive (upward) maximum due to entrainment near the bottom of the mixed layer. This implies a redistribution of the center of mass of the water column which results in an increase in the mean potential energy of the mixed layer. The near-surface structure in the buoyancy profiles seen in the low wind speed case is not observed here due to a high input of mechani-

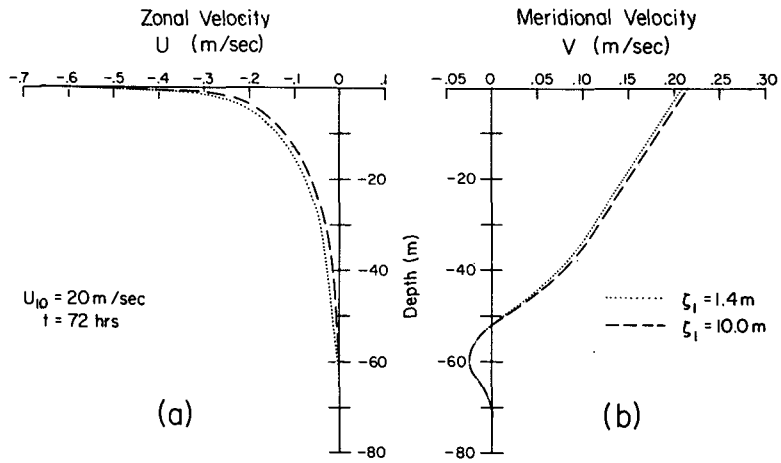

FIG. 11. Velocity profiles, analogous to those in Fig. 10, for a uniform speed of 20 m s^{-1}.

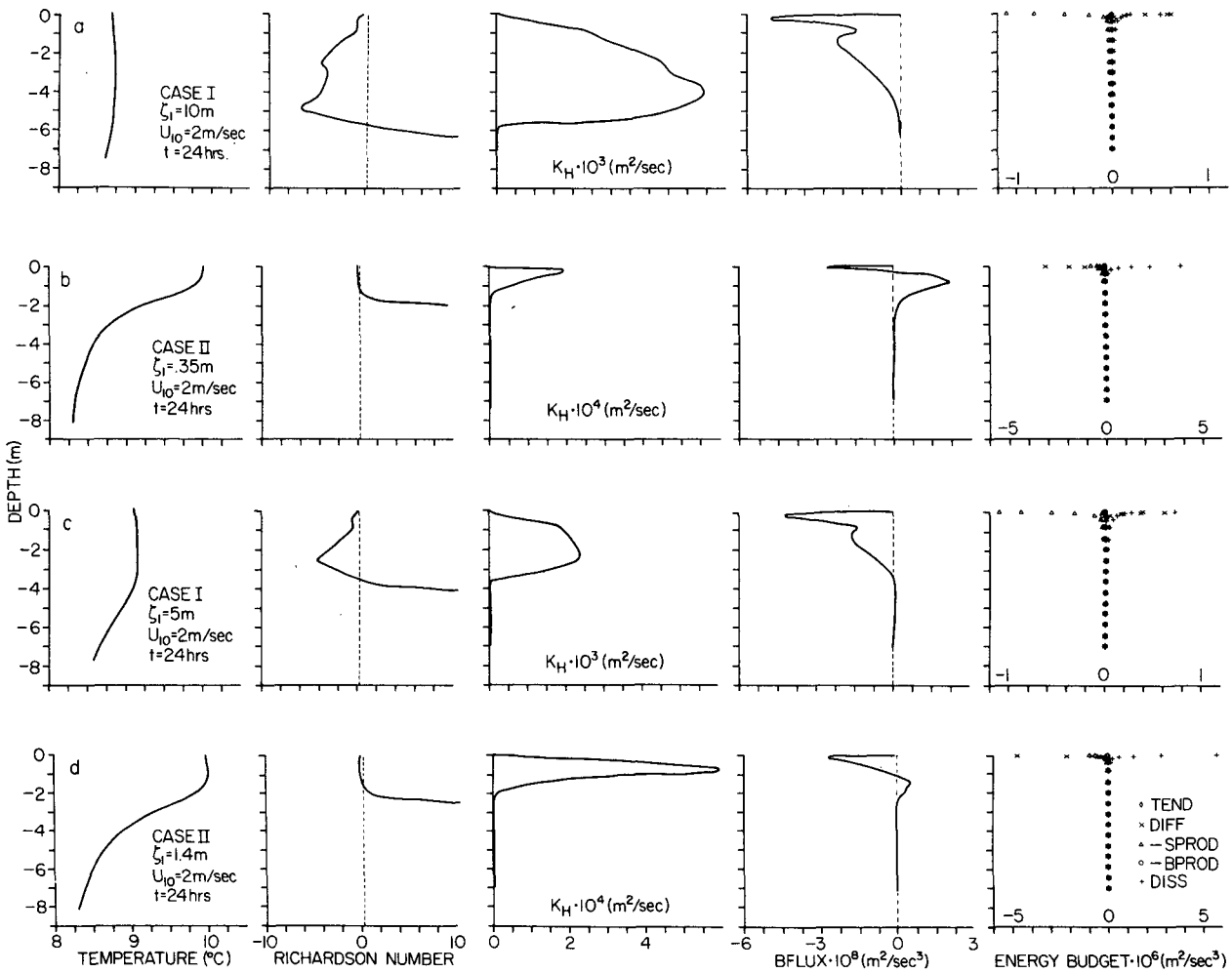

FIG. 12. Vertical profiles of temperature, flux Richardson number, eddy diffusivity of heat, buoyancy flux and the turbulent energy budget for all parameterizations at 24 h. U_{10} is 2 m s^{-1}.

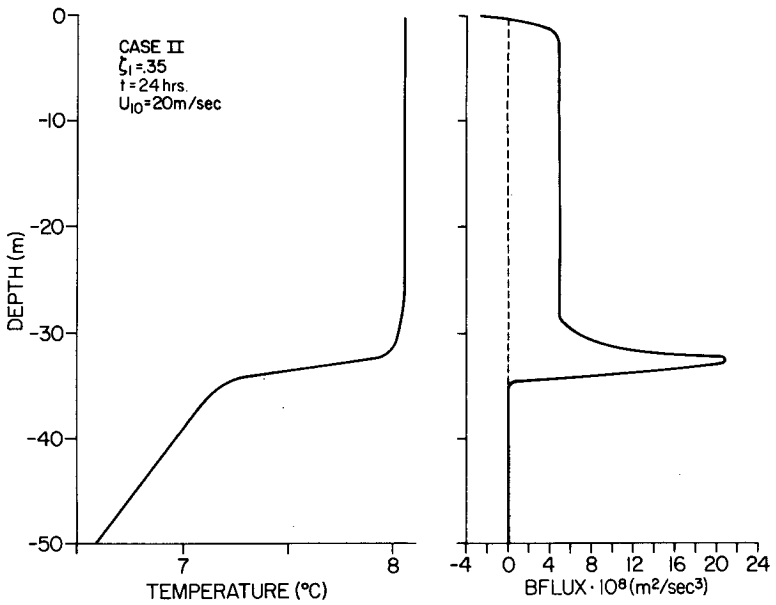

FIG. 13. Vertical profiles of temperature and buoyancy flux for case II (ζ_1 = 0.35 m) at 24 h. U_{10} is 20 m s^{-1}.

cal energy from the wind. The turbulent energy budget for high winds shows a balance between shear production and dissipation.

5. Summary

The effects of downward irradiance upon upper ocean structure were examined. A broad range of wind stress conditions and two general classes of irradiance parameterizations were used in the simulations. The first (case I) involved only one attenuation length, while the second (case II) utilized two attenuation lengths. The essential difference between the two classes of parameterizations was the vertical distribution of downward irradiance. The case II formulation provided for enhanced absorption of downward irradiance in the upper few meters. The Mellor-Yamada turbulent closure scheme (level 2½) was chosen for the study primarily on the basis of its capacity to allow for differential heating. The model was modified to include the effects of the penetrative components of solar radiation.

The case II parameterization resulted in warmer surface temperatures, shallower mixed layers, and more intense thermoclines than case I for wind speeds < 10 m s^{-1}. Case I was characterized by low sensitivity to variation in wind speed whereas case II featured a high degree of sensitivity to wind speed for $U_{10} > 1$ m s^{-1}.

Surface temperature (and mixed-layer depth) time series for the four parameterizations were compared. The relative order of the curves (each representing a given parameterization) changed as the wind speeds were increased from 0 to 10 m s^{-1}. This occurrence appeared to be related to the complex interplay between mixed-layer depth and the vertical distribution of downward irradiance. The simulations also indicated that the mean horizontal velocity is dependent on the particular empirical form of solar irradiance. This may be explained at least in part by the significant differences in the density structure.

For the low wind-speed case vertical profiles of the flux Richardson number and the eddy diffusivity of heat scale with the attenuation length ζ_1. In addition, a subsurface maximum occurs in the vertical profile of eddy diffusivity whose magnitude also scales with ζ_1. These two results are independent of parameterization. However, a more intense shear zone occurs at the base of the mixed layer for case II simulations which results in enhanced entrainment and a region of positive buoyancy flux near the bottom of the mixed layer. Regardless of parameterization, the turbulent energy budget is dominated by shear production, dissipation and the diffusion of turbulent kinetic energy.

All simulations under high wind speed conditions show nearly identical structure. In contrast to the low wind speed case, no near surface maximum in negative buoyancy flux occurs and an intense positive buoyancy flux is seen near the base of the mixed layer. For high winds, shear production is balanced by dissipation. It is felt that the results of these simulations provide evidence that downward irradiance and its proper parameterization are crucial to accurate predictions of upper ocean structure.

Acknowledgments. This research was supported by the Marine Life Research Group of the Scripps Institution of Oceanography and by the Institute for Marine and Coastal Studies and the Department of Geological Sciences of the University of Southern California. The authors wish to express their gratitude to Prof. George Mellor and Dr. Alan Blumberg for their valuable suggestions. Special thanks to Prof. J. L. Reid and Dr. Kern Kenyon for careful review of the preliminary manuscript. Sharon McBride typed the manuscripts and Kitty Kuhns provided editorial assistance. The figures were prepared by the MLRG Illustrations Group under the able direction of Fred Crowe. The constructive comments of the anonymous reviews were appreciated greatly.

REFERENCES

Alexander, R. C., and J.-W. Kim, 1976: Diagnostic model study of mixed layer depths in the summer North Pacific. *J. Phys. Oceanogr.*, **6**, 293–298.

Blumberg, A. F., and G. L. Mellor, 1978: A coastal ocean numerical model. *International Symposium on Mathematical Modelling of Estuarine Physics, Hamburg*, J. Sundermann, Ed., Springer-Verlag.

Clay, C. S., and H. Medwin, 1977: *Acoustical Oceanography, Principles and Applications.* Wiley, 544 pp.

Denman, K. L., 1973: A time-dependent model of the upper ocean. *J. Phys. Oceanogr.*, **3**, 173–184.

Denman, K. L., and M. Miyake, 1973: Upper layer modification at Ocean Station Papa: Observations and simulation. *J. Phys. Oceanogr.*, **3**, 185–196.

Eckart, C., 1968: *Principles and Applications of Underwater Sound.* Department of the Navy, NAVMAT P-9674 [Govt. Printing Office, Washington, DC].

Garwood, R. W., Jr., 1979: Air-sea interaction and dynamics of the surface mixed layer. *Rev. Geophys. Space Phys.*, **17**, 1507–1524.

Geisler, J. E., and E. B. Kraus, 1969: The well-mixed Ekman boundary layer. *Deep-Sea Res.*, **16** (Suppl.), 73–84.

Gill, A. E., and J. S. Turner, 1976: A comparison of seasonal thermocline models with observation. *Deep-Sea Res.*, **23**, 391–401.

Jerlov, N. G., 1968: *Optical Oceanography.* Elsevier, 194 pp.

Kitaigorodsky, S. A., and Y. Z. Miropolsky, 1970: On the theory of the open-ocean active layer. *Izv. Atmos. Oceanic Phys.*, **6**, 97–102.

Kondo, J., and I. Watabe, 1969: Seasonal changes of vertical profile of water temperature and evaporation from deep lakes (in Japanese with English abstract). *Rep. Nat. Res. Center Disaster Prevention*, **2**, 75–88.

——, Y. Sasano and T. Ishi, 1979: On wind-driven current and temperature profiles with diurnal period in the oceanic planetary boundary layer. *J. Phys. Oceanogr.*, **9**, 360–372.

Kraus, E. B., 1972: *Atmosphere-Ocean Interaction.* Clarendon Press, 275 pp.

——, 1977: *Modeling and Prediction of the Upper Layers of the Ocean.* Pergamon Press, 325 pp.

——, and C. Rooth, 1961: Temperature and steady state vertical heat flux in the ocean surface layer. *Tellus*, **13**, 231–238.

——, and J. S. Turner, 1967: A one-dimensional model of the seasonal thermocline: II. The general theory and its consequences. *Tellus*, **19**, 98–106.

Kundu, P. K., 1980: A numerical investigation of mixed-layer dynamics. *J. Phys. Oceanogr.*, **10**, 220–236.

List, R. L., 1951: *Smithsonian Meteorological Tables.* Smithsonian Institution, 527 pp.

Madsen, O. S., 1977: A realistic model of the wind-induced Ekman boundary layer. *J. Phys. Oceanogr.*, **7**, 248–255.

Marchuk, I. G., V. P. Kochergin, V. L. Klimok and V. A. Sukborukov, 1977: On the dynamics of the ocean surface mixed layer. *J. Phys. Oceanogr.*, **7**, 865–875.

McPhee, M. G., and J. D. Smith, 1976: Measurements of the turbulent boundary layer under pack ice. *J. Phys. Oceanogr.*, **6**, 696–711.

Mellor, G. L., 1973: Analytic prediction of the properties of stratified planetary surface layers. *J. Atmos. Sci.*, **30**, 1061–1069.

——, and T. Yamada, 1974: A hierarchy of turbulence closure models for planetary boundary layers. *J. Atmos. Sci.*, **31**, 1791–1806.

——, and P. A. Durbin, 1975: The structure and dynamics of the ocean surface mixed layer. *J. Phys. Oceanogr.*, **5**, 718–728.

——, and T. Yamada, 1977: A turbulence model applied to geophysical fluid problems. *Proceedings of the Symposium on Turbulent Shear Flows*, Pennsylvania State University Press, 1–14.

Niiler, P. P., 1975: Deepening of the wind-mixed layer. *J. Mar. Res.*, **33**, 405–427.

Paulson, C. A., and J. J. Simpson, 1977: Irradiance measurements in the upper ocean. *J. Phys. Oceanogr.*, **7**, 952–956.

Pollard, R. T., P. B. Rhines and R. O. R. Y. Thompson, 1973: The deepening of the wind-mixed layer. *Geophys. Fluid Dyn.*, **3**, 381–404.

Richtmyer, R. D., and K. W. Morton, 1967: *Difference Methods for Initial-Value Problems.* Interscience, 405 pp.

Simpson, J. J., and C. A. Paulson, 1977: Mixed layer observations during the NORPAX POLE Experiment: A data report. Oregon State University Data Rep. 66, Ref. 77-6, 167 pp.

——, and ——, 1979: Mid-ocean observations of atmospheric radiation. *Quart. J. Roy. Meteor. Soc.*, **105**, 487–502.

Sverdrup, H. U., M. W. Johnson and R. H. Fleming, 1942: *The Oceans: Their Physics, Chemistry and General Biology.* Prentice-Hall, 1087 pp.

Thompson, R. O. R. Y., 1976: Climatological numerical models of the surface mixed layer of the ocean. *J. Phys. Oceanogr.*, **6**, 496–503.

Yamada, T., 1977: A numerical experiment on pollutant dispersion in a horizontally-homogeneous atmospheric boundary layer. *Atmos. Environ.*, **11**, 1015–1024.